Continuum modelling of frequency dependent acoustic beam focusing and steering in hexagonal lattices

Giuseppe Rosi, Nicolas Auffray

Continuum modelling of frequency dependent acoustic beam focusing and steering in hexagonal lattices

G. Rosi[a,*], N. Auffray[b]

[a] *Université Paris-Est, Laboratoire Modélisation et Simulation Multi Echelle, MSME UMR 8208 CNRS, 61 av du Général de Gaulle, 94010 Créteil Cedex, France*

[b] *Université Paris-Est, Laboratoire Modélisation et Simulation Multi Echelle, MSME UMR 8208 CNRS, 5 bd Descartes, 77454 Marne-la-Vallée, France*

Abstract

Wave propagation in hexagonal lattices is characterised by a transition from isotropic to anisotropic regime as the frequency increases. This feature cannot be observed when the lattice material is modelled within the framework of classic Cauchy theory of elasticity, except when the real geometry of the microstructure is explicitly described. Homogenized equivalent continua can capture the onset of this anisotropy only if tensors involved in the constitutive law are at least of order six. This requirement is met in the case of Strain-Gradient Elasticity (SGE). In this work the SGE model is calibrated to quantitatively describe wave propagation within hexagonal lattices in a sufficiently large region of the dispersion diagram, by fitting the dispersion relations obtained from a Bloch-Floquet analysis on the unit cell. It is then shown that focussing and beam steering effects can be obtained by acting only on the local material orientation of the hexagonal lattice. This is achieved by computing the Poynting vector in the SGE model and optimising the distribution of material orientation.

Keywords: Strain-gradient elasticity, Anisotropy, Higher-order tensors, Beam steering, Wave propagation

1. Introduction

Defined by a constitutive material and an inner structure, Architectured Materials (AM) are halfway between bulk materials and structures. The organisation of the matter at intermediate scales opens new possibilities for material design (Ashby and Bréchet, 2003; Brechet and Embury, 2013), but also poses new challenges in modelling and simulation. Indeed, due to the possibly complex internal geometry of AMs, Direct Numerical Simulations (DNS, i.e. when the geometry of the inner structure is explicitly meshed in simulations) are often limited to

*Corresponding author

Email address: giuseppe.rosi@u-pec.fr (G. Rosi)

few unit cells, or few Representative Volume Elements (RVEs). Since AMs are often periodic, theirs elastodynamic behaviour can be captured by conducting the Floquet-Bloch analysis on the unit cell. When this approach is followed, computations restrict to only one unit cell and the complexity of the microstructure is usually not an issue.

However, this strategy only provides a satisfactory picture of waves propagating in an infinite periodic material. Aspects related to the finite size of the structure, such as for instance the influence of boundary conditions, cannot be described within this framework, nor can the pointwise modulation of the microstructure. In other words, this approach cannot be used for problems in which an actual sample made of AM is studied. To solve these technical difficulties, one possible strategy is to substitute the initial AM by a homogeneous material having *equivalent* effective properties. The *level of the equivalence* to consider depends mainly on the domain of application (i.e. statics or dynamics), the constraints of the specific problem and the level of complexity one intends to deal with. Typically, a compromise between these requirements is sought.

The more faithful effective models are constructed from non-local homogenisation schemes, such as the one initially developed by Willis (1997) and generalized by Nassar et al. (2015, 2016) and Sridhar et al. (2018). At the other end, the classical Cauchy homogenisation is too coarse to catch characteristic aspects of wave propagation in heterogeneous media such as dispersion, chirality or directivity.

Non-local effective models are difficult to be handled for practical applications, but they are effective to unveil the physical effects that can be achieved by controlling the local architecture of the matter. Among those effects, elastic cloaking is surely the one that retained most interest (Milton et al., 2006; Norris and Shuvalov, 2011). This effect consists in the possibility of bending elastic waves around a given region to make this region invisible (Zhou et al., 2012). Controlling wave propagation within a material by tailoring its microstructure has many practical applications ranging from fundation design in civil engineering (Rosi et al., 2018b) to biomechanics. However, the appealing physical properties predicted by non-local approaches resort on non-physical parameters, such as negative masses and stiffnesses (Liu et al., 251907). A question of practical importance is how to make these non-standard effects emerge from architectured materials without invoking non-physical parameters. Concerning different continuum modelling choices and their capabilities, a useful review is presented by Berezovski et al. (2013).

In this paper, we investigate approximate cloaking effect (more properly beam steering) that can be achieved by only controlling the orientation of the microstructure. This problem has

been studied in terms of optimisation of the unit cell by (Casadei and Rimoli, 2013; Chronopoulos, 2017; Zelhofer and Kochmann, 2017; Ruzzene et al., 2003) but, to authors' best knowledge, no local continuum model has been proposed to capture this phenomenon. For applications to optimal design, having a homogeneous overall description of the mechanical behaviour of AMs is of major interest. Such a model allows for obtaining analytical expressions of quantities of interest (e,g. propagation constants) that can be used in optimisation processes. However the correct choice for the overall continuum is not simple. As already mentioned, an effective classical Cauchy continuum is too poor to capture the dispersive nature of the wave propagation and a multitude of generalised models can be found in the literature, each one with its advantages and drawbacks. In this perspective, the questions one has to answer to determine a substitution continuum are the following:

- What is the domain (wave-lengths, frequency) over which the real material can be substituted by an equivalent one?
- Is there enough richness of information in this domain to justify the use of a generalised continuum?
- What are the features, in terms of wave propagation, that need to be preserved by the effective continuum?

In this paper, the main objective is to observe the onset of the dispersive behaviour of the material which lies outside the validity range of the classical Long Wavelength-Low Frequencies (LW-LF in the following) elastodynamics homogenisation scheme. As will be shown, in this region some non-standard effects such as frequency dependent anisotropic wave propagation and anisotropic inertial effects begin to emerge. As evidenced hereafter, these effects can be adequately captured by an overall strain-gradient elasticity model.

The paper is structured as follows. In section 2 elastic wave propagation in hexagonal lattices is discussed. This situation, which is geometrically simple, generates phenomena that cannot be reproduced by the classical LW-LF homogenisation scheme (Rosi and Auffray, 2016). As recently evidenced (Rosi et al., 2018a) in a certain range of length waves the situation can be accurately described within the realm of strain-gradient elasticity. The section 3 describes the main aspect of wave propagation within this framework. By the end of this section, numerical simulations are proposed to evidence that the salient features of heterogeneous wave propagation in hexagonal lattices are captured by the model. Finally, in section 4, an overall strain-gradient elastic material is used to conceive a frequency dependent beaming-device made of hexagonal

lattices.

Notations

In this work tensors of order ranking from 0 to 6 are denoted, respectively, by a, $\underline{\mathrm{a}}$, $\underset{\sim}{\mathrm{a}}$, $\underline{\underset{\sim}{\mathrm{a}}}$, $\underset{\approx}{\mathrm{a}}$, $\underline{\underset{\approx}{\mathrm{a}}}$ and $\underline{\underline{\underset{\approx}{\mathrm{a}}}}$. The simple, double and fourth-order contractions are written ., : and :: respectively. In index form, with respect to an orthonormal Cartesian basis, these notations correspond to:

$$\underline{\mathrm{a}} \cdot \underline{\mathrm{b}} = a_i b_i, \quad \underset{\sim}{\mathrm{a}} : \underset{\sim}{\mathrm{b}} = a_{ij} b_{ij}, \quad \underset{\approx}{\mathrm{a}} :: \underset{\approx}{\mathrm{b}} = a_{ijkl} b_{ijkl}, \qquad 1 \leq i, j, k, l \leq d$$

where repeated indices are summed up. Spatial gradient will classically be denoted, in index form, by a comma:

$$\mathrm{Grad}\ \underline{\mathrm{a}} = (\underline{\mathrm{a}} \otimes \underline{\nabla})_{ij} = a_{i,j}$$

When needed index symmetries are expressed as follows: (..) indicates invariance under permutations of the indices in parentheses, while $\underline{..}\ \underline{..}$ denotes invariance with respect to permutations of the underlined blocks. Finally, a superimposed dot will denote a partial time derivative.

The classical characteristic length scales of the model are:

- L_s: the scale of the specimen;
- L_i: the scale of the internal architecture (mesoscale);
- L_l: the loading wavelength;
- l_m: the scale of the constitutive microstructure[1].

All along the paper, the following assumptions have been made:

1. the influence of the sample size is neglected:

$$L_s \to \infty$$

2. The internal architecture is well-separated from the microscale, leading to the separation ratio assumption:

$$\frac{l_m}{L_i} \ll 1$$

[1]To be more precise, l_m is a length scale associated with the constituent material of which the architectured material is made. For a metal, this length can be the average grain size or for a polymer, the average size of polymer chains.

The specific position of an AM between a bulk material and a structure is indicated by the following ratio:

$$\eta = \frac{L_i}{L_l}$$

The value of η determines different characteristic regimes for architectured materials (AMs). Classic elasticity can be used only when $\eta \ll 1$, while for strain-gradient elasticity it has been shown in Rosi et al. (2018a) that the model is accurate for values up to $\eta = 1/6$. If $\eta \simeq 1$, the complete model must be used.

2. Wave propagation in hexagonal lattices

Honeycomb shaped microstructures are widely used and studied (Gibson and Ashby, 1999; Phani et al., 2006; Alderson et al., 2010; Liu et al., 2012). Numerous authors investigated the static and dynamic effective mechanical properties of this kind of materials. Before defining an overall continuum, we first consider, in this section, the wave propagation in the actual lattice by explicitly describing its microstructure. The dispersion properties of this architectured material will be used to calibrate the strain-gradient overall continuum model. The pattern under exam is presented in Figure 1, and it represents a 2D honeycomb geometry with unit cells of size[2] a and struts of thickness th. In this situation, the length scale of the mesostructure is characterized by a, hence $L_i = a$.

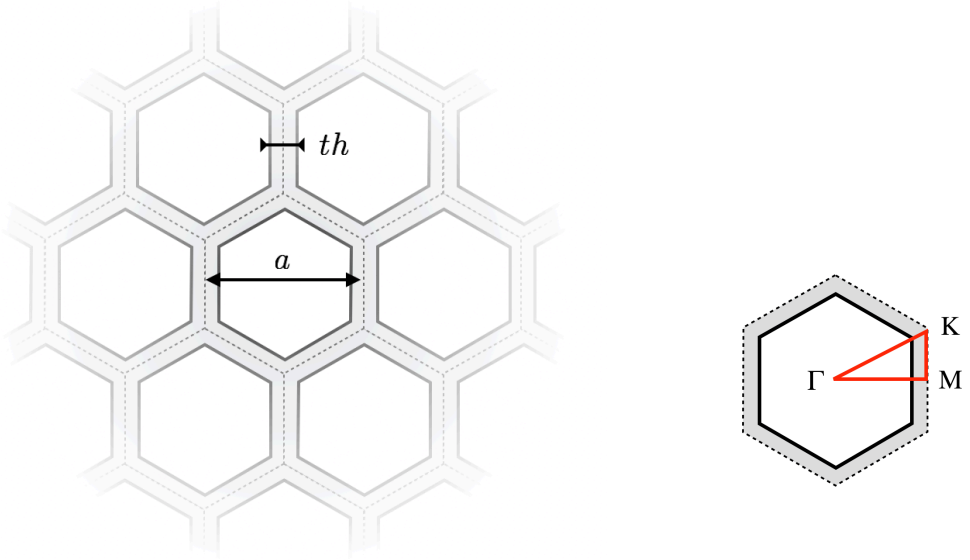

(a) Honeycomb lattice (b) Unit cell

Figure 1: Architectured D_6 Honeycomb (a) and unit cell with highlighted irreducible Brillouin zone (b).

[2]The size of the unit cell is defined as the diameter of the incircle of the hexagonal unit cell.

Consider the symmetries of the unit cell, its point group is conjugate to D_6 the dihedral group of order 12 (Forte and Vianello, 1996; Auffray et al., 2017). In words, the unit cell is invariant by $\frac{k\pi}{3}, k \in \mathbb{Z}$ rotations and possesses mirror lines of symmetry. In absence of mirror symmetries, the point group is restrained to Z_6 (the cyclic group of order 6) and correspond to the hexachiral pattern (Prall and Lakes, 1997; Dirrenberger et al., 2011; Bacigalupo and Gambarotta, 2014a) that will not be considered here.
The geometric parameters of the unit cell, as well as the material constants, are listed in Table 1.

a	1 mm	size of the unit cell
th	0.1 mm	size of the walls
E	20 GPa	Young's modulus
ν	0.3	Poisson ratio
ρ	2000 kg/m^3	mass density

Table 1: Material and geometric properties of the honeycomb material.

In this case study, the solid is modelled as a Cauchy continuum in plane strain. Quadratic Lagrange triangular elements are used, with a discretization size of 0.05mm. The dynamic signature of the AM is obtained by computing the dispersion diagram using the Floquet-Bloch theorem (Gazalet et al., 2013). The dispersion diagram following the edge of the Irreducible Brillouin Zone (defined in Figure 1) is presented in Figure 2. Following the results presented in (Rosi et al., 2018a), the target zone for a strain-gradient overall description corresponds to waves with a wavelength that is up to 6 times the size of the microstructure. In the present case, the size of the first Brillouin zone in the ΓM direction is $\pi/a = 6.28$ [rad/mm]. For simplicity, the validity range has been rounded to 2 [rad/mm]. As well known, elastic materials with hexagonal symmetries are isotropic in the plane, but this assumption is only valid for low values of the frequency (Rosi and Auffray, 2016). By zooming this area and superposing the ΓM and ΓK directions (right side of Figure 2), it can be observed that the model is slightly anisotropic, and that S-waves (the lower branch) are more affected than P-waves (the upper branch). This area is encircled in Figure 2(b).

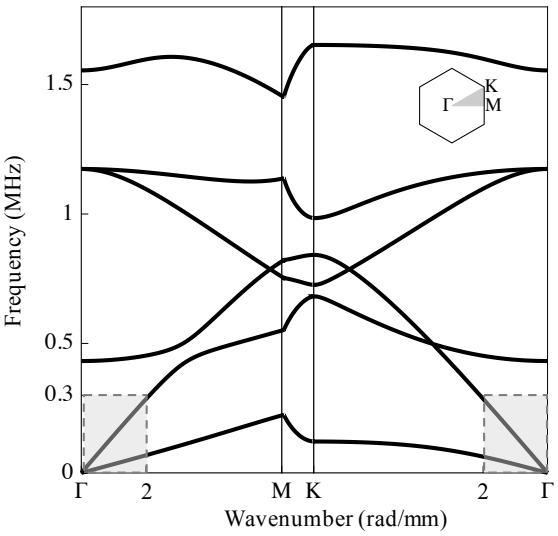

(a) Dispersion diagram for D_6 honeycomb lattice

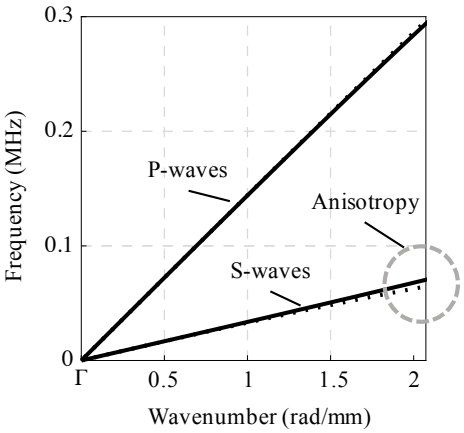

(b) Comparison of the initial part of ΓM (solid line) and ΓK (pointed line) paths

Figure 2: Global (a) and local (b) picture of the dispersion diagram for a hexagonal lattice.

Even if the anisotropy is not so marked, the effects on wave propagation, and especially on S-waves, are definitely not negligible. This can be observed by performing a time domain analysis of the propagation of a shear pulse in the honeycomb (as already discussed in Rosi and Auffray (2016)).

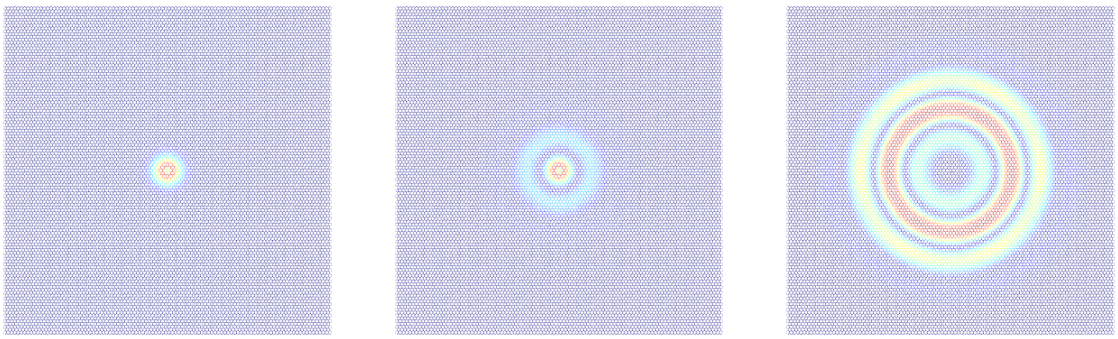

(a) t=20 μs (b) t=60 μs (c) t=100 μs

Figure 3: Snapshots at low frequency (20 Hz) for the honeycomb model ($\eta << 1$). The norm of the displacement is displayed, arbitrary units are used.

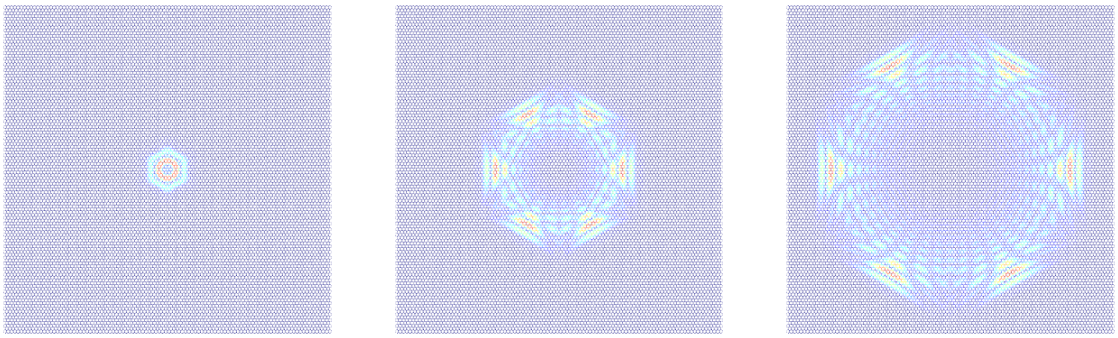

(a) t=20 μs (b) t=60 μs (c) t=100 μs

Figure 4: Snapshots at high frequency (90 kHz) for the honeycomb model ($\eta \simeq 6$). The norm of the displacement is displayed, arbitrary units are used.

In Figure 3 and Figure 4, the results of a Finite Elements Model (FEM) time domain simulation are shown. In this case, the AM is modeled as a 2D Cauchy continuum in plane strain. A shear pulse is applied in the center of the domain, and the total displacement is plotted. The central frequency of the pulse is 20 kHz for Figure 3 and 90 kHz for Figure 4. The higher frequency corresponds to the edge of the zone of validity of the SGE model (Figure 2). As can be observed, when the frequency increases, a symmetry transition emerges, with higher values of the displacement field concentrating in specific directions. This effect has already been shown in (Rosi and Auffray, 2016). In the next section the SGE model will be briefly recalled, and this phenomenon replicated in the case of a continuum model.

3. Strain-Gradient Elasticity

As usual in field theory of conservative systems, the Lagrangian density $\mathcal{L}$ is defined as the difference between the kinetic and potential energy densities, respectively, $\mathcal{K}$ and $\mathcal{P}$.

$$\mathcal{L} = \mathcal{K} - \mathcal{P}$$

In the case of Mindlin's Type II (Mindlin, 1964) SGE theory, these quantities are function of the displacement and its gradients up to the second-order:

$$\mathcal{K} = \frac{1}{2} p_i v_i + \frac{1}{2} q_{ij} v_{i,j}, \qquad \mathcal{P} = \frac{1}{2} \sigma_{ij} \varepsilon_{ij} + \frac{1}{2} \tau_{ijk} \eta_{ijk}.$$

The following quantities are involved in these definitions:

- p_i, and q_{ij} the momentum and the hypermomentum;
- v_i and $v_{i,j}$, the velocity ($v_i = \dot{u}_i$) and the spatial gradient of velocity;

- σ_{ij} and τ_{ijk}, the Cauchy stress and the hyperstress tensors;
- ε_{ij} and $\eta_{ijk} = \varepsilon_{ij,k}$, the infinitesimal strain tensor ($\varepsilon_{ij} = (u_{i,j} + u_{j,i})/2$) and its gradient.

With this choice of variables, the following *total* quantities can be defined:

- the total stress:

$$s_{ij} = \sigma_{ij} - \tau_{ijk,k} \tag{1}$$

- the total momentum:

$$\pi_i = p_i - q_{ik,k} \tag{2}$$

By application of the least action principle on the action functional (Mindlin, 1964; Auffray et al., 2015a), and neglecting body double force, the following bulk equations are obtained:

$$s_{ij,j} = \dot{p}_i - \dot{q}_{ij,j}. \tag{3}$$

3.1. Constitutive law

For the mechanical model to be closed, constitutive equations relating primal and dual quantities are mandatory. In the present situation, those relations will assumed to have the following structure:

$$\begin{pmatrix} \underline{\mathrm{p}} \\ \underset{\sim}{\mathrm{q}} \\ \underset{\sim}{\sigma} \\ \underset{\simeq}{\tau} \end{pmatrix} = \begin{pmatrix} \rho \underset{\sim}{\mathrm{I}} & \underset{\simeq}{\mathrm{K}} & 0 & 0 \\ \underset{\simeq}{\mathrm{K}}^T & \underset{\approx}{\mathrm{J}} & 0 & 0 \\ 0 & 0 & \underset{\approx}{\mathrm{C}} & \underset{\approx}{\mathrm{M}} \\ 0 & 0 & \underset{\approx}{\mathrm{M}}^T & \underset{\approx}{\mathrm{A}} \end{pmatrix} \begin{pmatrix} \underline{\mathrm{v}} \\ \underset{\sim}{\nabla \mathrm{v}} \\ \underset{\sim}{\varepsilon} \\ \underset{\simeq}{\eta} \end{pmatrix} \tag{4}$$

- $\rho I_{(ij)}$ is the macroscopic mass density;
- $K_{(ij)k}$ is the third-order tensor coupling linear momentum and hypermomentum tensor;
- $J_{(ij)qr}$ is the second-order inertia tensor;
- $C_{\underline{(ij)}\ \underline{(lm)}}$ is the classical elasticity tensor;
- $M_{(ij)(lm)n}$ is a fifth-order coupling elasticity tensor;
- $A_{\underline{(ij)k}\ \underline{(lm)n}}$ is a sixth-order elasticity tensor.

constitutive law can be simplified according to the invariance of the underlying matter. If the elementary cell is invariant with respect to the central inversion, the continuum is said to be centrosymmetric. In this situation, odd-order tensors vanish[3] and Eq.(4) simplifies to

$$\begin{pmatrix} \underline{\mathrm{p}} \\ \mathrm{q} \\ \underset{\sim}{\sigma} \\ \underline{\underline{\tau}} \end{pmatrix} = \begin{pmatrix} \rho \underset{\sim}{\mathrm{I}} & 0 & 0 & 0 \\ 0 & \underset{\approx}{\mathrm{J}} & 0 & 0 \\ 0 & 0 & \underset{\approx}{\mathrm{C}} & 0 \\ 0 & 0 & 0 & \underset{\approx\approx}{\mathrm{A}} \end{pmatrix} \begin{pmatrix} \underline{\mathrm{v}} \\ \nabla \mathrm{v} \\ \underset{\sim}{\varepsilon} \\ \underline{\underline{\eta}} \end{pmatrix} \tag{5}$$

The substitution of the constitutive equations into Eq.(1) and Eq.(2) gives:

$$\begin{aligned} s_{ij} &= C_{ijlm}\varepsilon_{lm} - A_{ijklmn}\varepsilon_{lm,kn}, \\ \pi_i &= \rho v_i - J_{ipqr}v_{q,pr}. \end{aligned}$$

Hence, for null body force, the bulk equilibrium (3) expressed in terms of the displacement field is:

$$C_{ijlm}u_{l,jm} - A_{ijklmn}u_{l,jkmn} = \rho\ddot{u}_i - J_{ipqr}\ddot{u}_{q,pr}. \tag{6}$$

3.2. Plane wave propagation and generalized acoustic tensor

Following the results presented in (Rosi and Auffray, 2016), let us consider the following plane wave solution

$$u_i = U_i\mathcal{A}\exp\left[\imath\omega\left(t - \frac{1}{V}\hat{\xi}_j x_j\right)\right] \tag{7}$$

where $V = \|\underline{\mathrm{v}}^p\|$ is the norm of the phase velocity of the wave-front and $\underline{\hat{\xi}}$ the unit vector pointing toward the direction of propagation, i.e. the normal to the wave-front. Moreover, U_i is a real valued unitary vector representing the polarization (direction of motion) and $\mathcal{A}$ is a complex amplitude. These quantities are independent of both x_i and t. The substitution of the ansatz (7) into the balance equation (6) yields

$$\left(\left(C_{ijlm} - \omega^2 J_{ijlm}\right)\hat{\xi}_j\hat{\xi}_m + \frac{\omega^2}{V^2}A_{ijklmn}\hat{\xi}_j\hat{\xi}_k\hat{\xi}_m\hat{\xi}_n\right)U_l = \rho V^2 U_i, \tag{8}$$

[3]Consider a n-th-order tensor T and $\mathrm{T}^\star$ its image by an isometric transformation. If the matter is invariant under a geometric transformation, so does its behaviour. In the case of a central inversion $\mathrm{T}^\star = (-1)^n\mathrm{T}$, hence the invariance condition can be written as :

$$(1 - (-1)^n)\mathrm{T} = 0$$

which implies the vanishing of T for odd order tensors ($n = 2p + 1$).

which can be conveniently rewritten as

$$\hat{Q}_{il}U_l = \rho V^2 U_i, \tag{9}$$

where the generalized acoustic tensor $\hat{Q}_{il}$ is defined as follows:

$$\hat{Q}_{il} = \left(C_{ijlm} - \omega^2 J_{ijlm}\right)\hat{\xi}_j\hat{\xi}_m + \frac{\omega^2}{V^2}A_{ijklmn}\hat{\xi}_j\hat{\xi}_k\hat{\xi}_m\hat{\xi}_n. \tag{10}$$

The expression for the group velocity can be obtained. This quantity is defined as

$$\underline{\mathrm{v}}^g = \frac{\partial\omega}{\partial\underline{\mathrm{k}}} \tag{11}$$

where $\underline{\mathrm{k}}$ is the wavevector. From equation (10) it can be shown that

$$v_j^g = \frac{Q^\sharp_{ijl}U_lU_i}{V\left(\rho\delta_{ik} + \frac{\omega^2}{V^2}J_{ijkl}\hat{\xi}_j\hat{\xi}_l\right)U_kU_i} \tag{12}$$

where

$$Q^\sharp_{ijl} = \left(C_{ijlm} - \omega^2 J_{ijlm}\right)\hat{\xi}_m + \frac{\omega^2}{V^2}A^\sharp_{ijklmn}\hat{\xi}_k\hat{\xi}_m\hat{\xi}_n,$$

and

$$A^\sharp_{ijklmn} = \left(A_{ikjlmn} + A_{ijklmn}\right) \tag{13}$$

In order to investigate energy flow within the material, the Poynting vector should be used (Brillouin, 1960; Bacigalupo and Lepidi, 2018). To that aim, we consider the local form of the conservation of energy

$$\frac{\partial\mathcal{E}}{\partial t} + P_{i,i} = 0,$$

in this expression $\underline{\mathrm{P}}$ denotes the Poynting vector. Using the constitutive equations (5), and the conservation of linear momentum (3) its general expression can be specified:

$$P_j = -\left(s_{ij} + \dot{q}_{ij}\right)\dot{u}_i - \tau_{ikj}\dot{u}_{i,k}.$$

Inserting the plane wave solution (7) into this last expression and performing a temporal averaging,

$$\langle\cdot\rangle = \frac{1}{T}\int_0^T \cdot\,\mathrm{d}t$$

the following result is obtained.

$$\langle P_j\rangle = \frac{|\mathcal{A}|^2}{2}\frac{\omega^2}{V}Q^\flat_{ijl}U_lU_i \tag{14}$$

in which the following tensors have been introduced

$$Q^\flat_{ijl} = \left(C_{ijlm} - \omega^2 J_{ijlm}\right)\hat{\xi}_m - \frac{\omega^2}{V^2}A^\flat_{ijklmn}\hat{\xi}_k\hat{\xi}_m\hat{\xi}_n,$$

with

$$A^\flat_{ijklmn} = \left(A_{ijklmn} - A_{ikjlmn}\right).$$

3.3. Constitutive law for a hexagonal lattice

The overall constitutive relations are now specified for the considered hexagonal lattice (c.f. Figure 1). To define the constitutive law the higher-order stiffness tensors have to be defined together with the higher-inertia tensors. Concerning the first point, the description of all the anisotropic strain-gradient elastic systems can be found in (Auffray et al., 2015b, 2018). The classification detailed in this reference is based on the point group of the unit cell. As discussed in section 2, the symmetry class of the unit cell of the considered lattice is D_6. For the considered material symmetry class, the generalized elastic law has the following structure:

$$\begin{pmatrix} \underset{\sim}{\sigma} \\ \underset{\simeq}{\tau} \end{pmatrix} = \begin{pmatrix} \underset{\approx}{\mathrm{C}}^{\mathrm{O}(2)} & 0 \\ 0 & \underset{\approx\approx}{\mathrm{A}}^{\mathrm{D}_6} \end{pmatrix} \begin{pmatrix} \underset{\sim}{\varepsilon} \\ \underset{\simeq}{\eta} \end{pmatrix} \tag{15}$$

In which $\underset{\approx}{\mathrm{C}}^{\mathrm{O}(2)}$ stands for the isotropic elasticity tensor, and $\underset{\approx\approx}{\mathrm{A}}^{\mathrm{D}_6}$ for a second-order anisotropic elasticity tensor.

Using the Kelvin matrix notation for representing higher-order tensors in matricial form (c.f. Appendix A) $\underset{\approx}{\mathrm{C}}^{\mathrm{O}(2)}$ has the following shape:

$$\underset{\approx}{\mathrm{C}}^{\mathrm{O}(2)} = \begin{pmatrix} c_P & c_P - 2c_S & 0 \\ c_P - 2c_S & c_P & 0 \\ 0 & 0 & 2c_S \end{pmatrix}_{\mathcal{K}} \tag{16}$$

with

$$c_P = \lambda + 2\mu \quad ; \quad c_S = \mu$$

being the P-wave modulus and the shear modulus, respectively. The second-order elasticity tensor $\underset{\approx\approx}{\mathrm{A}}$ is anisotropic for hexagonal unit-cell. However this anisotropy does not increase by far the complexity of the model, since the anisotropic tensor only departs from the isotropic one by one coefficient. In the following expressions, Θ represents the angle of the unit cell with respect to the axis $\underset{\sim}{\mathrm{e}}_1$ (a graphical representation of the angle is presented in subsection 4.1, Figure 10). Using an adapted Kelvin notation $\underset{\approx\approx}{\mathrm{A}}^{\mathrm{D}_6}$ (c.f. Appendix A) has the following structure:

$$\underset{\approx\approx}{\mathrm{A}}^{\mathrm{D}_6}(\Theta) = \underset{\approx\approx}{\mathrm{A}}^{\mathrm{O}(2)} + a_D \underset{\approx\approx}{\mathrm{A}}(\Theta) \tag{17}$$

with

$$\underset{\approx\approx}{\mathrm{A}}^{\mathrm{O}(2)} = \begin{pmatrix} a_{11} & a_{12} & \frac{\sqrt{2}}{2}(a_{11}-a_{22})-a_{23} & 0 & 0 & 0 \\ a_{12} & a_{22} & a_{23} & 0 & 0 & 0 \\ \frac{\sqrt{2}}{2}(a_{11}-a_{22})-a_{23} & a_{23} & \frac{1}{2}(a_{11}+a_{22})-a_{12} & 0 & 0 & 0 \\ 0 & 0 & 0 & a_{11} & a_{12} & \frac{\sqrt{2}}{2}(a_{11}-a_{22})-a_{23} \\ 0 & 0 & 0 & a_{12} & a_{22} & a_{23} \\ 0 & 0 & 0 & \frac{\sqrt{2}}{2}(a_{11}-a_{22})-a_{23} & a_{23} & \frac{1}{2}(a_{11}+a_{22})-a_{12} \end{pmatrix}_{\mathcal{K}}$$

$$\underset{\approx\approx}{\mathrm{A}}(\Theta) = \cos(6\Theta) \begin{pmatrix} 1 & -1 & -\sqrt{2} & 0 & 0 & 0 \\ -1 & 1 & \sqrt{2} & 0 & 0 & 0 \\ -\sqrt{2} & \sqrt{2} & 2 & 0 & 0 & 0 \\ 0 & 0 & 0 & -1 & 1 & \sqrt{2} \\ 0 & 0 & 0 & 1 & -1 & -\sqrt{2} \\ 0 & 0 & 0 & \sqrt{2} & -\sqrt{2} & -2 \end{pmatrix}_{\mathcal{K}} + \sin(6\Theta) \begin{pmatrix} 0 & 0 & 0 & -1 & 1 & \sqrt{2} \\ 0 & 0 & 0 & 1 & -1 & -\sqrt{2} \\ 0 & 0 & 0 & \sqrt{2} & -\sqrt{2} & -2 \\ 1 & -1 & -\sqrt{2} & 0 & 0 & 0 \\ -1 & 1 & \sqrt{2} & 0 & 0 & 0 \\ -\sqrt{2} & \sqrt{2} & 2 & 0 & 0 & 0 \end{pmatrix}_{\mathcal{K}}$$

Thus, with respect to the isotropic case, only one additional coefficient is introduced (a_D), which is responsible for the symmetry transition. The form of $\underset{\approx\approx}{\mathrm{A}}^{\mathrm{D}_6}$ presented in Auffray et al. (2015b) can be retreived by considering $\Theta = 0$ and $a_D = a_{44} - a_{11}$. Higher-order stiffnesses have to be supplemented by higher-order inertia. In the present situation, this means considering the second-order inertia tensor $\underset{\approx}{\mathrm{J}}$. Its index symmetries are considered according to the asymptotic construction provided in Bacigalupo and Gambarotta (2014b) and correspond to the classical minor and major symmetries of the elasticity tensor. Hence, for a hexagonal cell, $\underset{\approx}{\mathrm{J}}$ is isotropic and defined by two generalized "Lamé" parameters: κ, γ:

$$J_{ijkl} = \kappa\delta_{ij}\delta_{kl} + \gamma(\delta_{ik}\delta_{jl} + \delta_{il}\delta_{jk})$$

This inertia tensor obtained in Bacigalupo and Gambarotta (2014b) differs from the one constructed phenomenologically by Mindlin (1964). In this last reference the isotropic system is defined by only one coefficient. Numerical simulations (not detailed here) showed that this option was not satisfactory. Using the Kelvin matrix notation, $\underset{\approx}{\mathrm{J}}^{\mathrm{O}(2)}$ has the following form:

$$\underset{\approx}{\mathrm{J}}^{\mathrm{O}(2)} = \begin{pmatrix} j_P & j_P - 2j_S & 0 \\ j_P - 2j_S & j_P & 0 \\ 0 & 0 & 2j_S \end{pmatrix}_{\mathcal{B}} \tag{18}$$

with

$$j_P = \kappa + 2\gamma \quad ; \quad j_S = \gamma$$

3.4. Calibration and validation of the model

The constants of the model have been calculated by fitting the group velocity computed from Bloch analysis, following partially the method introduced and detailed in Rosi et al. (2018a). In the cited contribution identification was two-step: 1) static experiments to determine, first, the higher-order stiffnesses then, 2) dynamic experiments to evaluate the contribution of higher-order inertia. This identification procedure has the advantage of giving a unique set of constitutive coefficients, but of course must be performed in two steps. In order to perform a one step identification, a purely dynamic identification must be preferred. However, when computing phase and group velocity for a bulk plane wave, one can notice that only a reduced set of coefficients appears in their expression. This can be shown by considering a plane wave with unitary wave vector $\hat{\xi} = (\cos(\theta), \sin(\theta))$, where θ is the angle with respect to e_1 and injecting the expressions (16), (17) and (18) in equation (8). For a material orientation $\Theta = 0$, the directions $\theta = 0$ rad and $\theta = \pi/6$ rad coincide with the mirror lines of the unit cell, and the resulting expressions for the phase and group velocities are provided in Table 2.

θ	Phase velocity P	Group Velocity P	Phase velocity S	Group Velocity S
0	$\sqrt{\frac{c_P + a_P k^2}{\rho + j_P k^2}}$	$\frac{k^2 a_P (j_P k^2 + 2\rho) + c_P \rho}{(j_P k^2 + \rho)^{3/2} \sqrt{k^2 a_P + c_P}}$	$\sqrt{\frac{c_S + (a_S/4 + a_D) k^2}{\rho + j_S k^2}}$	$\frac{k^2 (a_D + a_S/4)(j_S k^2 + 2\rho) + c_S \rho}{(j_S k^2 + \rho)^{3/2} \sqrt{k^2 (a_D + a_S/4) + c_P}}$
$\frac{\pi}{6}$	$\sqrt{\frac{c_P + (a_P + a_D) k^2}{\rho + j_P k^2}}$	$\frac{k^2 (a_D + a_P)(j_P k^2 + 2\rho) + c_P \rho}{(j_P k^2 + \rho)^{3/2} \sqrt{k^2 (a_D + a_P) + c_P}}$	$\sqrt{\frac{c_S + (a_S/4) k^2}{\rho + j_S k^2}}$	$\frac{k^2 a_S/4 (j_S k^2 + 2\rho) + c_S \rho}{(j_S k^2 + \rho)^{3/2} \sqrt{k^2 a_S/4 + c_P}}$

Table 2: Phase and group velocities along characteristic directions of the unit cell ($\theta = 0, \pi/6$)

In these expressions, the parameters a_P and a_S are defined as:

$$a_P = a_{11}, \qquad a_S = a_{11} + a_{22} - 2a_{12}. \tag{19}$$

and they are related to the isotropic contribution of the sixth-order elasticity tensor. The coefficient a_{23} does not appear at all in the expressions of phase and group velocities. However, this coefficient intervenes when considering particular boundary conditions, or in the case of guided propagation (Georgiadis et al., 2000; Gourgiotis and Georgiadis, 2015; Eremeyev et al., 2018). Indeed, in order to obtain a unique set of parameters, a boundary value problem must be considered (e.g. guided propagation Vavva et al. (2009) or reflection problems (dell'Isola et al., 2011; Gourgiotis et al., 2013)).

In the present work, a novel dynamic identification procedure based on guided propagation is used. The Floquet-Bloch analysis of the unit cell of a plate having a hexagonal microstructure with the parameters listed in Table 1 and a thickness of 15mm has been used to obtain the plate dispersion curves. Then the generalised Rayleigh-Lamb equation for SGE was numerically

solved and the solution fitted with the results from the Floquet-Bloch analysis. This procedure has the advantage of involving Neumann boundary conditions on the free boundary and thus allow for the identifications of all the coefficients. This identification procedure is complex and will be the object of a forthcoming paper. The results of the fitting are summarised in Table 3. As it can be remarked, the values of the anisotropic contribution a_D is two orders of magnitude larger than the isotropic one.

c_P	c_S	ρ	a_{11}	a_{22}	a_{44}	a_{23}	a_{12}	a_P	a_S	a_D	j_P	j_S
[GPa]	[MPa]	[kg/m ^{3}]	[N]	[N]	[N]	[N]	[N]	[N]	[N]	[N]	[kg/m]	[kg/m]
1.25	67.4	380.	0.04	0.03	13.87	0.02	0.00	0.04	0.49	13.83	$7.10 \cdot 10^{-5}$	$6.42 \cdot 10^{-5}$

Table 3: Constitutive coefficients obtained from the fitting procedure.

Since shear waves have a more pronounced anisotropic behaviour, the analysis is restricted to this kind of waves. In Figure 5, the polar plots of phase and group velocities of S-waves are shown for different values of the frequencies. The transition from isotropic to anisotropic behaviour when the frequency increases can be noticed and the good fit with the Floquet-Bloch analysis can be appreciated.

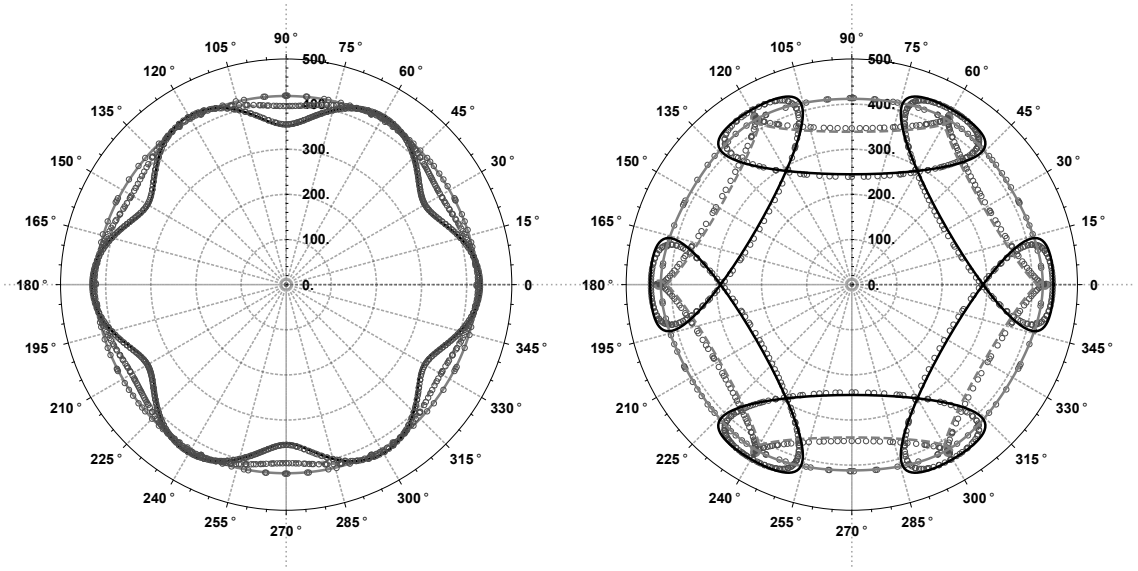

(a) Phase velocity

(b) Group velocity

Figure 5: Polar plots of the fitted phase and group velocities for different values of the frequency: 20 kHz (solid gray), 60 kHz (dashed gray), 90 kHz (solid black). The gray circles are the points obtained from the Floquet-Bloch analysis.

3.5. Bulk propagation

The model calibrated in the previous section is here tested in a dynamic framework, and compared to the results presented in section 2. In this case, the simulation has been conducted

using an anisotropic SGE elasticity model implemented on Comsol Multiphysics and using third-order Hermite elements for the interpolation of the displacement field. A discretization size of 1mm is considered. The computation domain is of finite size with Dirichlet conditions on the boundary. In the lack of Perfectly Matched Layers (PML), and to avoid spurious reflections on the boundary of Ω, the time interval used for the simulation is limited. The shear source is located at the center of the domain, its central frequency can be chosen in order to produce either low (c.f. Figure 6) or high (c.f. Figure 7) frequency elastic waves. For comparison, the solution obtained when considering a classic Cauchy continuum is in Figure 8. As expected, the classic model, being isotropic, fails in predicting the correct response.

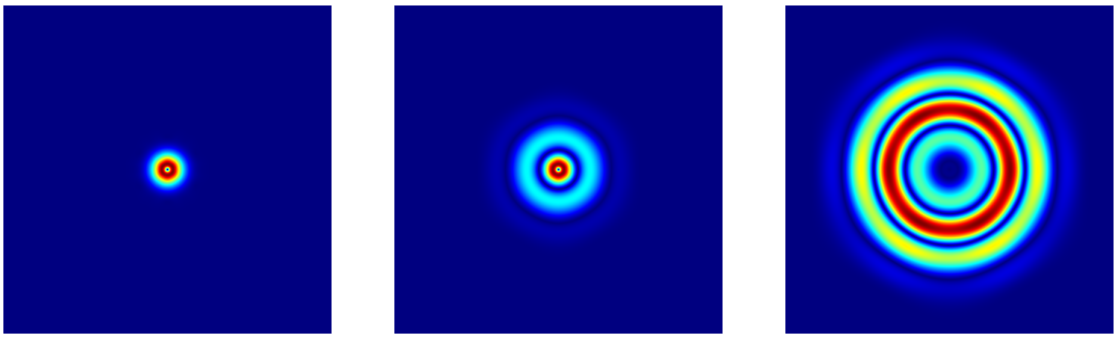

(a) t=20 μs (b) t=60 μs (c) t=100 μs

Figure 6: Snapshots of wave propagation for a low value of the exciting frequency (20 kHz) using a strain-gradient calibrated model. Total displacement is displayed.

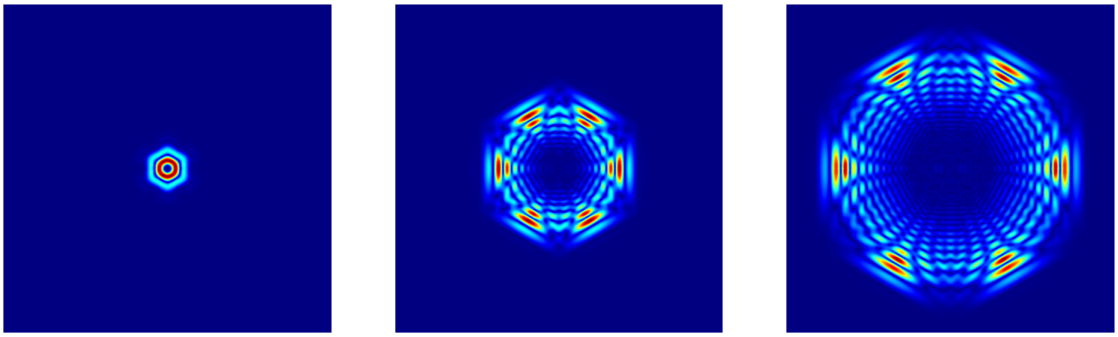

(a) t=20 μs (b) t=60 μs (c) t=100 μs

Figure 7: Snapshots of wave propagation for a high value of the exciting frequency (90 kHz) using a strain-gradient calibrated model. Total displacement is displayed.

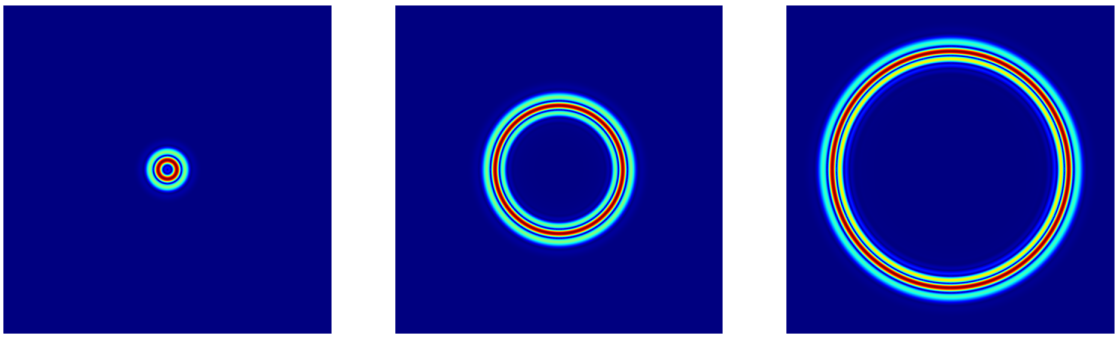

(a) t=20 μs (b) t=60 μs (c) t=100 μs

Figure 8: Snapshots of wave propagation for a high value of the exciting frequency (90 kHz) using a classic Cauchy model. Total displacement is displayed.

3.6. Frequency dependent deviation of the Poynting vector

As previously discussed in Rosi and Auffray (2016), the frequency dependent directivity that has been observed in discrete lattice (c.f. Figure 4) can be nicely captured and reproduced using a strain-gradient elastic continuum. It worth emphasising that, in the framework of SGE, this anisotropic phenomenon just departs from the isotropic situation by one extra coefficient. As shown in subsection 3.2, once the constitutive parameters are determined, the Poynting vector can be computed by using Equation 14. As illustrated in Figure 9, the direction of Poynting vector depends both on the frequency and on the direction of propagation $\hat{\underline{\xi}}$. When the wavevector $\hat{\underline{\xi}}$ spans the angles from 0 to 2π, the tip of the Poynting vector draws ellipses around the tip of the wave vector, forming the ripples visible in Figure Figure 9. This feature will be used in the next section to control elastic wave propagation along a predefined frequency dependent path.

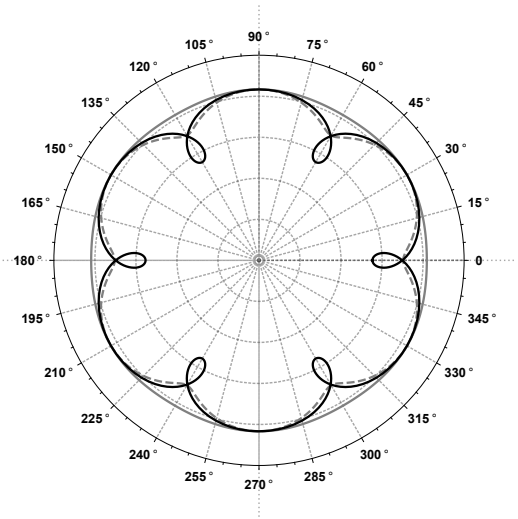

Figure 9: Effect of the frequency on the Poynting vector: 20 kHz (solid gray), 60 kHz (dashed gray), 90 kHz (solid black). The amplitude of the Poynting vector is normalised with respect to the maximum value of its norm.

4. Application to beam steering and focusing

In this section an application is shown, where the computation of the Poynting vector introduced in subsection 3.2 is required.

4.1. Frequency dependent deviation of the Poynting vector

The following notation will be used for the angles, defined with respect to $\underline{e}_1$:

- θ is the orientation of the wavevector;
- Θ is orientation of the unit cell (material orientation);
- θ_P is orientation of the Poynting vector.

A schematic representation of the angles for $\theta = 0$ is in Figure 10.

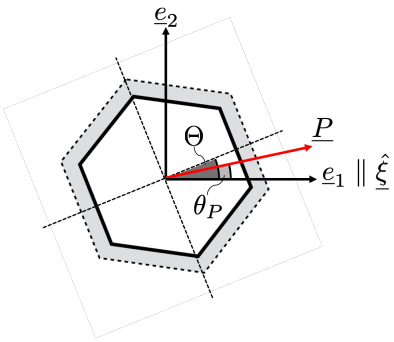

Figure 10: Schematic representation of the angles involved. In this picture $\theta = 0$.

In what follows, we will fix the value of θ to zero, i.e. the wavevector is fixed and parallel to $\underline{e}_1$, while changing the material orientation Θ. In this case, it can be observed that the tip of the Poynting vector draws ellipses around the wavevector, and that the vector itself is confined within angular sector centred around $\hat{\underline{\xi}}$. This phenomenon can be observed in Figure 11, for a central frequency of 90kHz. The opening of the sector is an increasing function of the frequency, as illustrated in Figure 12 and Figure 13.

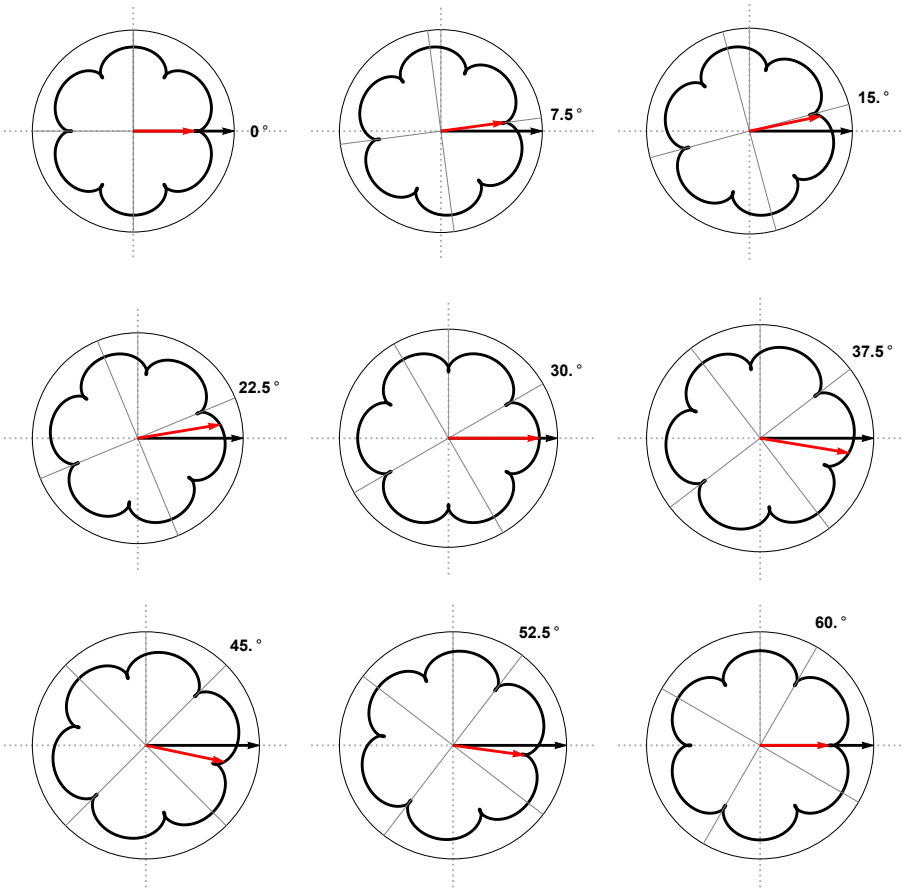

Figure 11: Poynting vector (red arrow, colors online) for different values of Θ, as indicated in the right part of every subplot, and $f = 90$kHz

Hence, for every frequency within the validity range of the model, it can be found an optimal material orientation Θ_{opt} that maximises the deviation of the Poynting vector θ_P. The result of this computation for different values of the frequency is presented in Table 4.

Frequency [kHz]	Θ_{opt} [deg]	θ_P [deg]
20	15.1	0.5
30	15.2	1.2
40	15.3	2.3
50	15.5	3.7
60	15.7	5.7
70	16.0	8.4
80	16.3	12.0
90	16.7	16.7

Table 4: The values of the material orientation angle for which the maximum deflection of the Poynting vector is achieved.

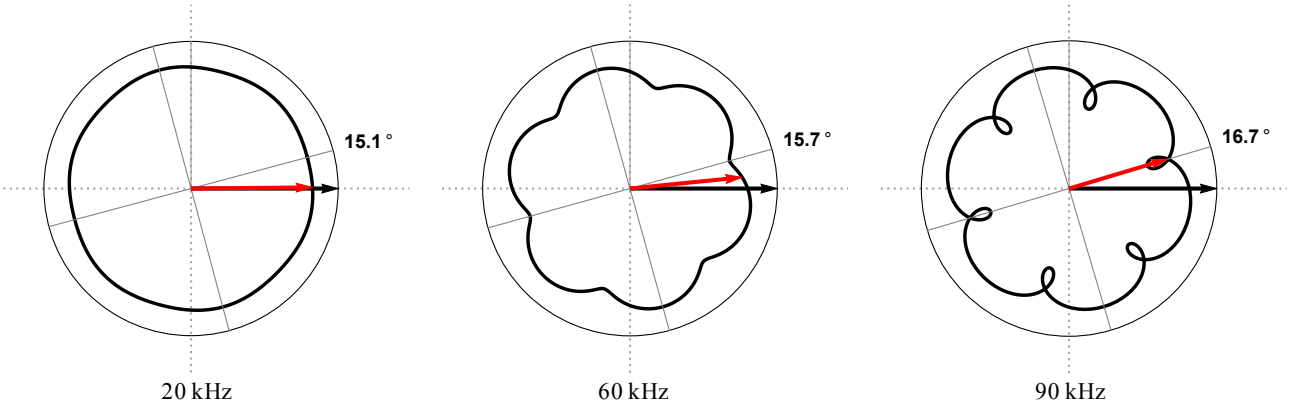

Figure 12: Polar plots of the normalised Poynting vector (red arrow, colors online) corresponding to a wave propagating towards direction $\underline{\xi}$ indicated by the black arrow.

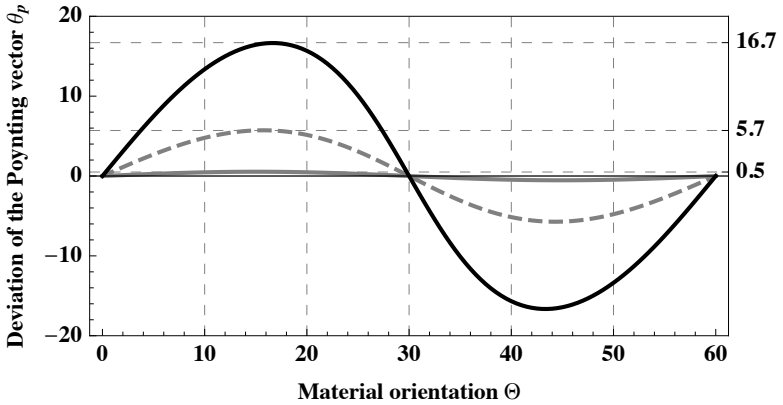

Figure 13: Effect of the frequency on the deviation of the Poynting vector: 20 kHz (solid gray), 60 kHz (dashed gray), 90 kHz (solid black).

4.2. Bending and focussing waves without affecting the wavevector

As an illustration, we designed an architectured material that deviates elastic waves at a certain frequency. The specimen is a rectangular domain, measuring 200 × 100mm. The specimen is illustrated in Figure 14. Upper and lower boundaries are clamped (vanishing displacement and normal derivative of the displacement), the left and right boundaries are free (vanishing traction and hypertraction, see Rosi et al. (2018a) for more details about boundary conditions in SGE). In this example, in order to "avoid" the hole, the energy must steer with an angle that is greater than 12 deg. From the results presented in the previous section, this can be achieved by imposing $\Theta_{opt} = 16$ deg and a central frequency of 70 kHz. In order to minimise the dispersion effects the minimum value for the frequency that allows for a desired deviation θ_p has been chosen. Then, the field of the material orientation that optimises the steering has been chosen in this form

$$\Theta_{opt}(x_1) = \Theta_{opt} \sin(\pi \frac{2x_1 - L}{L}). \tag{20}$$

An illustration of the orientation distribution in the domain is presented in Figure 15. It is important to remark that, at this stage, this distribution is not the result of an optimisation based on an objective function. The reformulation of the problem into a true optimization problem, in order to investigate more general configurations, will be the object of further studies.

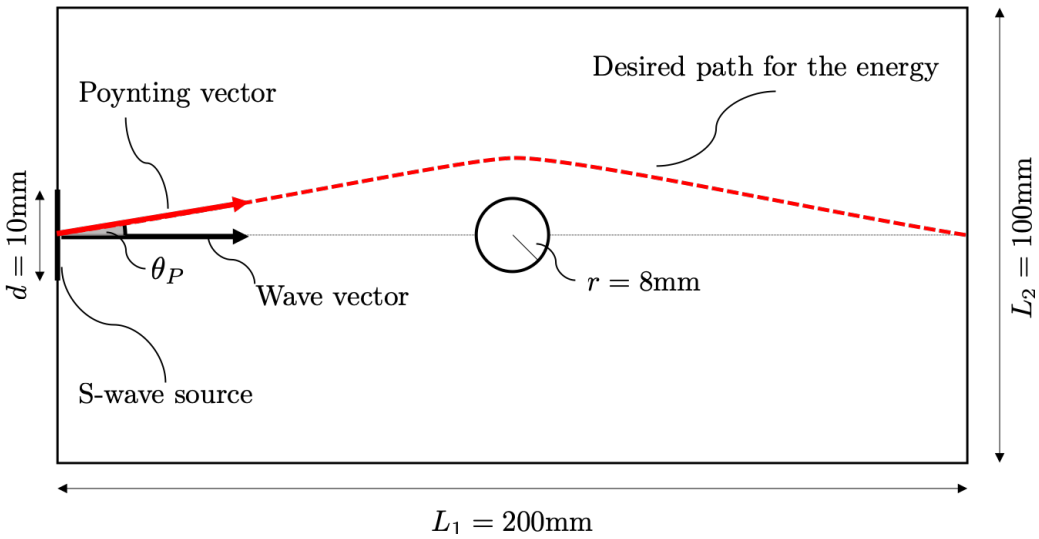

Figure 14: Schematic description of the specimen and of the desired path for the energy.

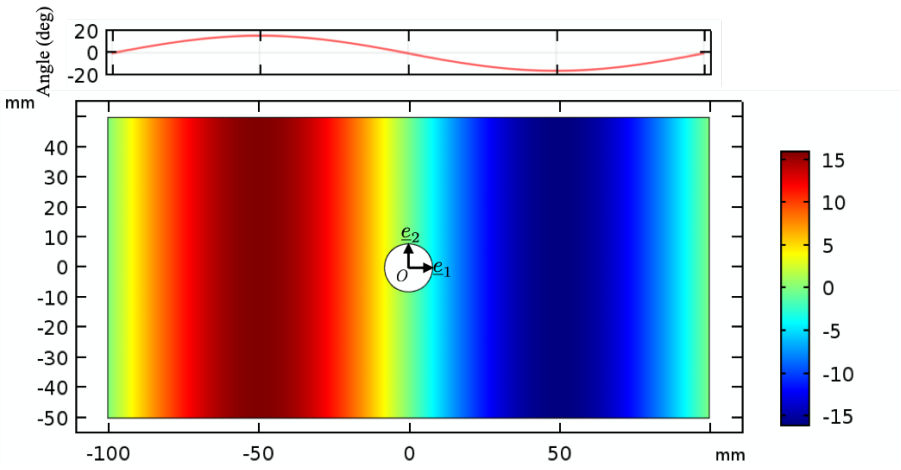

Figure 15: Optimal distribution of the material orientation angle $\Theta_{opt}(x_1)$.

In Figure 16 the results of a time domain simulations are presented. The source is a shear sine burst applied at the left boundary by imposing a vertical displacement at the source (Figure 14) of size $d = 10$ mm, in order to generate a plane wave. When the material orientation is constant (i.e. for $\Theta = 0$), the elastic wave beam scatters massively on the hole. Most of the elastic energy is back scattered, and a receptor located on the right boundary will only measure some perturbations of the displacement field (Figure 16(a)), or the reflections on the clamped boundary. When the optimal distribution $\Theta_{opt}(x_1)$ is introduced the beam deviates. However, as can be seen in Figure 16(b), the wavenumber remains horizontal, since only the Poynting vector is affected by this change in the material orientation. Scattering is considerably decreased, as the majority of the energy is deviated and does not interact with the hole. Indeed, most of the elastic energy is guided and focussed, and a receptor located on the right boundary will receive a clean signal.

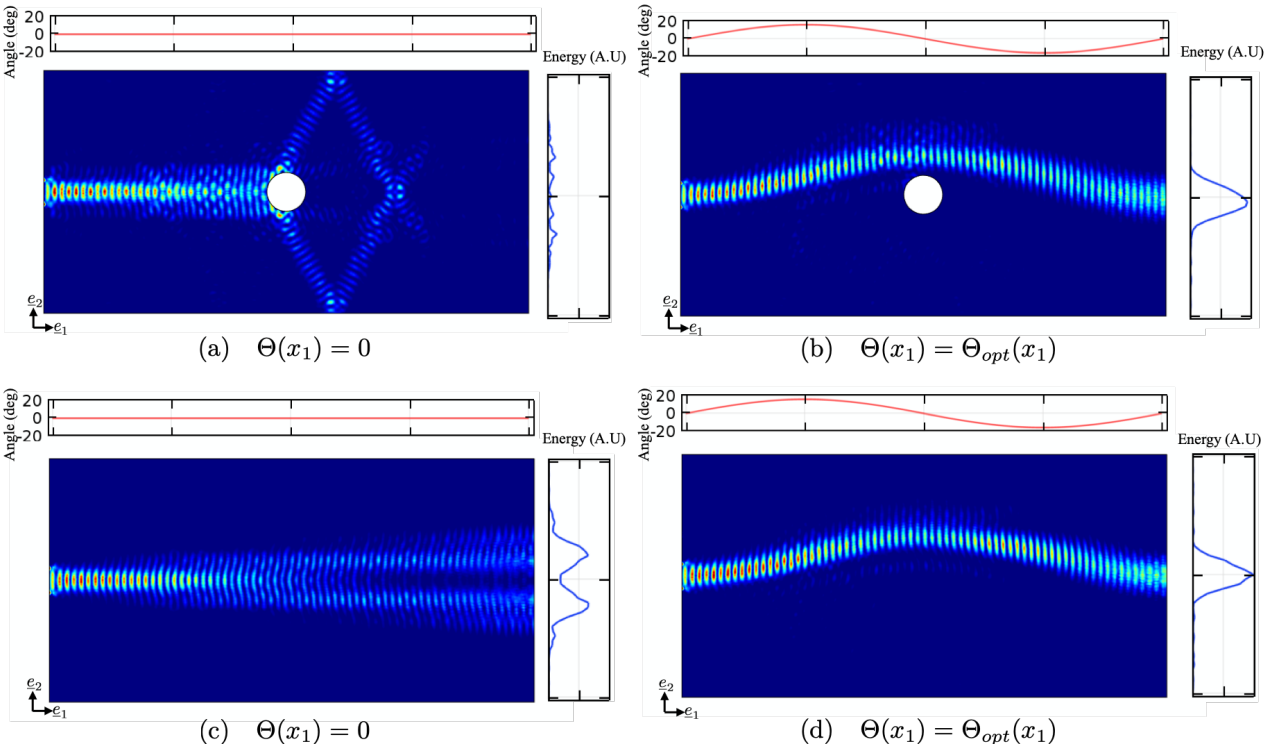

Figure 16: Four different case studies. On the left of each image the distribution of the energy at $t = 700\mu$s , on the right of each image the energy received at the right side of the specimen, in arbitrary units. Above each image the function $\Theta_{opt}(x_1)$ is plotted.

Moreover, a focussing effect can be observed when the energy is guided by the change of the material orientation. To illustrate this phenomenon, let us consider the experimental setting as described previously, except that now the hole has been removed from the numerical sample. For the first numerical experiment the material orientation is uniformly equal to zero within the specimen (i.e $\Theta = 0$) and the result of the numerical simulation is reported on Figure 16(c). The measure of the transmitted signal is symmetric and shows two major energy peaks. This is due to the dispersive nature of wave propagation in the medium. This effect can also be observed in bulk wave propagation from a point source presented in subsection 3.5.

Now let consider the optimal distribution of material orientation $\Theta_{opt}(x_1)$. The result of the numerical simulation is reported on Figure 16(d). For the frequency considered in the simulation the beam is bent, and the resulting transmitted signal is symmetric and shows a unique energy peak. The path control we impose has restricted the transverse spread of the wave packet. This focussing effect is frequency dependent. The result is very close to the one obtained for a specimen with a hole (Figure 16(b)), showing that the steering of the energy is effective.

Conclusion

In this paper we presented results concerning elastic wave propagation in hexagonal lattices. We showed that the SGE model can be used to capture the anisotropic wave propagation occurring when the frequency increases, and that a reduced set of constitutive parameters is needed to calibrate the model. Then, an application to beam steering in architectured materials is shown.

The main results presented in this work are the following:

- A decomposition of the sixth-order constitutive tensor of SGE model for the hexagonal symmetry is used. It is highlighted that a single coefficient is sensitive to material orientation Θ.
- The SGE model is calibrated using the Floquet-Bloch analysis. Time domain analysis is used to verify the calibration.
- A steering effect is achieved by acting the material orientation at the macro-scale. The optimal orientation distribution is obtained from the computation of the Poynting vector in SGE.
- A focussing effect is observed when the wave propagates in the architectured material with the optimal orientation distribution.

Further extensions of this work will concern simulations of the actual architectured material with the optimal orientation profile. Experimental evidences to the described phenomena of steering and focussing will be also sought. A detailed description of the identification procedure based on guided propagation will be the object of a forthcoming paper. Concerning the modelling process, the effect of boundaries and a more refined identification procedure allowing to uniquely compute all the independent set of coefficients, involving homogenisation techniques, are envisaged.

Acknowledgments

The authors thanks the *International Research Program Coss&Vita* for the support *via* "Fédération Francilienne de Mécanique, CNRS FR2609". Giuseppe Rosi has been supported by the CNRS through the PEPS program "HipImpact". The authors thank the reviewers for their fruitful comments.

Appendix A. Kelvin notation

To express higher-order tensors using matrix notations we will define two basis such as

$$\widetilde{\mathbf{C}} = \sum_{I,J=1,1}^{3,3} \widetilde{C}_{IJ} \widetilde{\underline{\mathrm{e}}}_I \otimes \widetilde{\underline{\mathrm{e}}}_J \quad \widehat{\mathbf{A}} = \sum_{\alpha,\beta=1,1}^{6,6} \widehat{A}_{\alpha\beta} \widehat{\underline{\mathrm{e}}}_\alpha \otimes \widehat{\underline{\mathrm{e}}}_\beta, \tag{A.1}$$

The basis vectors are defined by

$$\begin{aligned} \widetilde{\underline{\mathrm{e}}}_I &= \left(\frac{1-\delta_{ij}}{\sqrt{2}} + \frac{\delta_{ij}}{2} \right) \left(\underline{\mathrm{e}}_i \otimes \underline{\mathrm{e}}_j + \underline{\mathrm{e}}_j \otimes \underline{\mathrm{e}}_i \right), \quad 1 \leq I \leq 3 \\ \widehat{\underline{\mathrm{e}}}_\alpha &= \left(\frac{1-\delta_{ij}}{\sqrt{2}} + \frac{\delta_{ij}}{2} \right) \left(\underline{\mathrm{e}}_i \otimes \underline{\mathrm{e}}_j + \underline{\mathrm{e}}_j \otimes \underline{\mathrm{e}}_i \right) \otimes \underline{\mathrm{e}}_k, \quad 1 \leq \alpha \leq 6 \end{aligned}$$

where the summation convention for a repeated subscript does not apply. The obtained bases will be denoted as $\mathcal{K}$, in order to distinguish them from the physical bases. Using these bases the different tensors can be expressed as:

$$\widetilde{\underline{\varepsilon}} = \sum_{I=1}^{3} \widetilde{\varepsilon}_I \widetilde{\underline{\mathrm{e}}}_I, \quad \widetilde{\sigma} = \sum_{I=1}^{3} \widetilde{\sigma}_I \widetilde{\underline{\mathrm{e}}}_I, \quad \widehat{\underline{\eta}} = \sum_{\alpha=1}^{6} \widehat{\eta}_\alpha \widehat{\underline{\mathrm{e}}}_\alpha, \quad \widehat{\underline{\tau}} = \sum_{\alpha=1}^{6} \widehat{\tau}_\alpha \widehat{\underline{\mathrm{e}}}_\alpha \tag{A.2}$$

so that the strain-gradient constitutive law can be written

$$\begin{cases} \widetilde{\sigma}_I = \widetilde{C}_{IJ} \widetilde{\varepsilon}_J + \overline{M}_{I\alpha} \widehat{\eta}_\alpha \\ \widehat{\tau}_\alpha = \overline{M}_{\alpha J} \widetilde{\varepsilon}_J + \widetilde{A}_{\alpha\beta} \widehat{\eta}_\beta \end{cases} \tag{A.3}$$

The relationship between the matrix components $\widetilde{\varepsilon}_I$ and ε_{ij}, and between $\widehat{\eta}_\alpha$ and η_{ijk} are

$$\widetilde{\varepsilon}_I = \begin{cases} \varepsilon_{ij} \ \text{ if } \ i = j, \\ \sqrt{2}\varepsilon_{ij} \ \text{ if } \ i \neq j; \end{cases} \qquad \widehat{\eta}_\alpha = \begin{cases} \eta_{ijk} \ \text{ if } \ i = j, \\ \sqrt{2}\eta_{ijk} \ \text{ if } \ i \neq j; \end{cases} \tag{A.4}$$

and, obviously, the same relations between $\widetilde{\sigma}_I$ and σ_{ij} and $\widehat{\tau}_\alpha$ and τ_{ijk} hold. For the constitutive tensors we have the following correspondences:

$$\widetilde{C}_{IJ} = \begin{cases} C_{ijkl} \ \text{ if } \ i = j \text{ and } k = l, \\ \sqrt{2}C_{ijkl} \ \text{ if } \ i \neq j \text{ and } k = l \text{ or } i = j \text{ and } k \neq l, \\ 2C_{ijkl} \ \text{ if } \ i \neq j \text{ and } k \neq l. \end{cases} \tag{A.5}$$

$$\widehat{A}_{\alpha\beta} = \begin{cases} A_{ijklmn} \ \text{ if } \ i = j \text{ and } l = m, \\ \sqrt{2}A_{ijklmn} \ \text{ if } \ i \neq j \text{ and } l = m \text{ or } i = j \text{ and } l \neq m, \\ 2A_{ijklmn} \ \text{ if } \ i \neq j \text{ and } l \neq m. \end{cases} \tag{A.6}$$

It remains to choose appropriate two-to-one and three-to-one subscript correspondences between ij and I, on one hand, and ijk and α, on the other hand. For the classical variables the standard two-to-one subscript correspondence is used, i.e:

I	1	2	3
ij	11	22	12

Table A.5: The two-to-one subscript correspondence for 2D strain/stress tensors

The three-to-one subscript correspondence for strain-gradient/hyperstress tensor, specified in Table 5.

α	1	2	3	4	5	6
ijk	111	221	122	222	112	121

Table A.6: The three-to-one subscript correspondence for 2D strain-gradient/hyperstress tensors

This results in the following matrix representations for the considered tensors:

$$\underset{\approx}{\mathrm{C}} = \begin{pmatrix} c_{1111} & c_{1122} & \sqrt{2}c_{1112} \\ c_{1122} & c_{2222} & \sqrt{2}c_{2212} \\ \sqrt{2}c_{1112} & \sqrt{2}c_{2212} & 2c_{1212} \end{pmatrix}_{\mathcal{K}} \tag{A.7}$$

$$\underset{\approx}{\mathrm{A}} = \begin{pmatrix} a_{111111} & a_{111221} & \sqrt{2}a_{111122} & a_{111222} & a_{111112} & \sqrt{2}a_{111121} \\ a_{221111} & a_{221221} & \sqrt{2}a_{221122} & a_{221222} & a_{221112} & \sqrt{2}a_{221121} \\ \sqrt{2}a_{122111} & \sqrt{2}a_{122221} & 2a_{122122} & \sqrt{2}a_{122222} & \sqrt{2}a_{122112} & 2a_{122121} \\ a_{111222} & a_{221222} & \sqrt{2}a_{122222} & a_{222222} & a_{222112} & \sqrt{2}a_{222121} \\ a_{111112} & a_{221112} & \sqrt{2}a_{122112} & a_{122222} & a_{122112} & \sqrt{2}a_{122121} \\ \sqrt{2}a_{111121} & \sqrt{2}a_{221121} & 2a_{122121} & \sqrt{2}a_{121222} & \sqrt{2}a_{121112} & 2a_{121121} \end{pmatrix}_{\mathcal{K}} \tag{A.8}$$

References

Alderson, A., Alderson, K. L., Attard, D., Evans, K. E., Gatt, R., Grima, J. N., Miller, W., Ravirala, N., Smith, C. W., Zied, K., 2010. Elastic constants of 3-, 4- and 6-connected chiral and anti-chiral honeycombs subject to uniaxial in-plane loading. Composites Science and Technology 70 (7), 1042–1048.

Ashby, M. F., Bréchet, Y., 2003. Designing hybrid materials. Acta materialia 51 (19), 5801–5821.

Auffray, N., dell'Isola, F., Eremeyev, V., Madeo, A., Rosi, G., 2015a. Analytical continuum mechanics à la hamilton–piola least action principle for second gradient continua and capillary fluids. Mathematics and Mechanics of Solids 20 (4), 375–417.

Auffray, N., Dirrenberger, J., Rosi, G., 2015b. A complete description of bi-dimensional anisotropic strain-gradient elasticity. International Journal of Solids and Structures 69, 195–206.

Auffray, N., He, Q.-C., Le Quang, H., 2018. Complete symmetry classification and compact matrix representations for 3D strain gradient elasticity. International Journal of Solids and Structures On-line.

Auffray, N., Kolev, B., Olive, M., 2017. Handbook of bi-dimensional tensors: Part I: Harmonic decomposition and symmetry classes. Mathematics and Mechanics of Solids 22 (9), 1847–1865.

Bacigalupo, A., Gambarotta, L., 2014a. Homogenization of periodic hexa- and tetrachiral cellular solids. Composite Structures 116, 461–476.

Bacigalupo, A., Gambarotta, L., 2014b. Second-gradient homogenized model for wave propagation in heterogeneous periodic media. International Journal of Solids and Structures 51 (5), 1052–1065.

Bacigalupo, A., Lepidi, M., 2018. Acoustic wave polarization and energy flow in periodic beam lattice materials. International Journal of Solids and Structures.

Berezovski, A., Engelbrecht, J., Salupere, A., Tamm, K., Peets, T., 2013. Dispersive waves in microstructured solids. International Journal of Solids and Structures 50 (11), 1981–1990.

Brechet, Y., Embury, J. D., 2013. Architectured materials: expanding materials space. Scripta Materialia 68 (1), 1–3.

Brillouin, L., 1960. Wave Propagation and Group Velocity. Vol. 191. Academic Press.

Casadei, F., Rimoli, J. J., May 2013. Anisotropy-induced broadband stress wave steering in periodic lattices. International Journal of Solids and Structures 50 (9), 1402–1414.

Chronopoulos, D., Jan. 2017. Wave steering effects in anisotropic composite structures: Direct calculation of the energy skew angle through a finite element scheme. Ultrasonics 73, 43–48.

dell'Isola, F., Madeo, A., Placidi, L., Dec. 2011. Linear plane wave propagation and normal transmission and reflection at discontinuity surfaces in second gradient 3D continua. ZAMM - Journal of Applied Mathematics and Mechanics / Zeitschrift für Angewandte Mathematik und Mechanik 92 (1), 52–71.

Dirrenberger, J., Forest, S., Jeulin, D., Colin, C., 2011. Homogenization of periodic auxetic materials. Procedia Engineering 10, 1847–1852.

Eremeyev, V. A., Rosi, G., Naili, S., May 2018. Comparison of anti-plane surface waves in strain-gradient materials and materials with surface stresses. Mathematics and Mechanics of Solids 42, 108128651876996.

Forte, S., Vianello, M., 1996. Symmetry classes for elasticity tensors. Journal of Elasticity 43 (2), 81–108.

Gazalet, J., Dupont, S., Kastelik, J.-C., Rolland, Q., Djafari-Rouhani, B., 2013. A tutorial survey on waves propagating in periodic media: Electronic, photonic and phononic crystals. perception of the bloch theorem in both real and fourier domains. Wave Motion 50 (3), 619–654.

Georgiadis, H. G., Vardoulakis, I., Lykotrafitis, G., May 2000. Torsional surface waves in a gradient-elastic half-space. Wave Motion 31 (4), 333–348.

Gibson, L. J., Ashby, M. F., 1999. Cellular solids: structure and properties. Cambridge university press.

Gourgiotis, P., Georgiadis, H., Neocleous, I., 2013. On the reflection of waves in half-spaces of microstructured materials governed by dipolar gradient elasticity. Wave Motion 50 (3), 437–455.

Gourgiotis, P. A., Georgiadis, H. G., Jun. 2015. Torsional and SH surface waves in an isotropic and homogenous elastic half-space characterized by the Toupin–Mindlin gradient theory. International Journal of Solids and Structures 62, 217–228.

Liu, X., Huang, G., Hu, G., 2012. Chiral effect in plane isotropic micropolar elasticity and its application to chiral lattices. Journal of the Mechanics and Physics of Solids 60 (11), 1907–1921.

Liu, X. N., Hu, G. K., Huang, G. L., Sun, C. T., 251907. An elastic metamaterial with simultaneously negative mass density and bulk modulus. Applied Physics Letters 98 (25), 5246–5250.

Milton, G. W., Briane, M., Willis, J. R., 2006. On cloaking for elasticity and physical equations with a transformation invariant form. New Journal of Physics 8 (10), 248.

Mindlin, R., 1964. Micro-structure in linear elasticity. Archive for Rational Mechanics and Analysis 16 (1), 51–78.

Nassar, H., He, Q.-C., Auffray, N., 2015. Willis elastodynamic homogenization theory revisited for periodic media. Journal of the Mechanics and Physics of Solids 77, 158–178.

Nassar, H., He, Q.-C., Auffray, N., 2016. A generalized theory of elastodynamic homogenization for periodic media. International Journal of Solids and Structures 84, 139–146.

Norris, A., Shuvalov, A., Sep. 2011. Elastic cloaking theory. Wave Motion 48 (6), 525–538.

Phani, A., Woodhouse, J., Fleck, N., 2006. Wave propagation in two-dimensional periodic lattices. The Journal of the Acoustical Society of America 119 (4), 1995.

Prall, D., Lakes, R., 1997. Properties of a chiral honeycomb with a poisson's ratio of -1. International Journal of Mechanical Sciences 39 (3), 305–314.

Rosi, G., Auffray, N., 2016. Anisotropic and dispersive wave propagation within strain-gradient framework. Wave Motion 63, 120–134.

Rosi, G., Placidi, L., Auffray, N., May 2018a. On the validity range of strain-gradient elasticity: A mixed static-dynamic identification procedure. European Journal Of Mechanics A-Solids 69, 179–191.

Rosi, G., Ropars, P., Auffray, N., 2018b. New mitigation solution by waves deviation, numerical experiments. In: Euronoise.

Ruzzene, M., Scarpa, F., Soranna, F., 2003. Wave beaming effects in two-dimensional cellular structures. Smart materials and structures 12 (3), 363.

Sridhar, A., Kouznetsova, V., Geers, M., 2018. A general multiscale framework for the emergent effective elastodynamics of metamaterials. Journal of the Mechanics and Physics of Solids 111, 414–433.

Vavva, M. G., Protopappas, V. C., Gergidis, L. N., Charalambopoulos, A., Fotiadis, D. I., Polyzos, D., May 2009. Velocity dispersion of guided waves propagating in a free gradient elastic plate: Application to cortical bone. The Journal of the Acoustical Society of America 125 (5), 3414.

Willis, J., 1997. Dynamics of composites. In: Suquet, P. (Ed.), Continuum Micromechanics. Springer-Verlag, New York, Ch. Dynamics of composites, pp. 265–290.

Zelhofer, A. J., Kochmann, D. M., Jun. 2017. On acoustic wave beaming in two-dimensional structural lattices. International Journal of Solids and Structures 115–116, 248–269.

Zhou, X., Liu, X., Hu, G., 2012. Elastic metamaterials with local resonances: an overview. Theoretical and Applied Mechanics Letters 2 (4).